

Extreme Value Analysis for Peak Heliostat Wind Load Predictions

Matthew Emes¹[\[https://orcid.org/0000-0003-4147-4387\]](https://orcid.org/0000-0003-4147-4387), Bruce Leslie², and Maziar Arjomandi¹

¹ The University of Adelaide, Adelaide SA 5005, Australia.

² Vast Solar, Goodna QLD 4300, Australia.

Abstract. This study investigated high-frequency load fluctuations on a rectangular heliostat model in a boundary layer wind tunnel experiment. Statistical methods for peak wind load predictions were compared with load distributions through load cell and surface pressure measurements on the heliostat model placed in two simulated atmospheric boundary layers (ABLs) representing a flat desert terrain and open country terrain. It was found that statistical peak predictions based on horizontal wind gust velocity amplitude underestimates the load coefficients in stow and at oblique azimuth angles for maximum azimuth moments. In addition, it was shown that the distributions of the centre of pressure position and the hinge moment in stow position are non-Gaussian. It is therefore recommended that the frequency and amplitude of the vertical wind velocity component must be considered for peak load predictions of hinge moments and azimuth moments.

Keywords: Heliostat Wind Load, Solar Thermal Energy, Atmospheric Boundary Layer

1. Introduction

Turbulence due to high-amplitude wind gusts in the lowest 10 meters of the atmospheric boundary layer (ABL) can generate considerably higher loads above their mean values on heliostat components. To estimate the maximum wind loads in different heliostat orientations and structural configurations Extreme Value Analysis of fluctuating wind loads based on quasi-static theory is applied to load time series data. Peterka and Derickson [1] reported the aerodynamic coefficients of the forces and moments on a conventional azimuth-elevation heliostat. Wind load coefficients were calculated following quasi-static theory applied to high-frequency force balance measurements in simulated ABL wind tunnel experiments and the mean wind speed at the elevation axis height of a scale-model heliostat.

Analysis of transient load distributions on a scale-model heliostat in the University of Adelaide wind tunnel using the three-sigma approach adopted in the equivalent static wind load design methods implemented by Peterka and Derickson [1] was found to underpredict the maximum hinge moment about the central elevation axis and overturning moment about the base of the pedestal [2]. Further, positive skewness of the von Mises combined stress distributions on the pedestal and torque tube calculated from the measured loads resulted in the three-sigma peak of the Gaussian distribution being underestimated by 6% and 2%, respectively, in comparison with a cumulative probability of 99.7% of the best-fit Gaussian distribution [3]. Hence, this study aims to evaluate the three-sigma and gust factor methods for calculating peak load coefficients on a heliostat model in a turbulent ABL and identify the most accurate method for calculating the wind loads on heliostats.

The equivalent static wind loads on heliostats can be determined based on the recommendations from the design codes and provisions for buildings that the peak aerodynamic loads are the sum of the mean load F_{mean} and three times the standard deviation σ_F of the load fluctuations with a 99.7% probability of the three-sigma peak values not being exceeded for an assumed Gaussian distribution [4]

$$F_{peak} = F_{mean} + 3\sigma_F \quad (1)$$

The gust factor approach can be used to estimate the ratio of the peak loads to the mean loads due to the atmospheric turbulence with assumed negligible contribution of self-induced turbulence due to the body shape [5, 6]

$$F_{peak} = F_{mean}(1+2k_u I_u) \quad (2)$$

Here k_u is the peak factor (= 3 for a 3-second gust wind speed and mean wind speed averaging time of 1 hour [6]) and $I_u = \sigma_u/U_{mean}$ is the turbulence intensity defined by the ratio of the standard deviation of the longitudinal velocity component and the mean velocity at the heliostat elevation axis height. The objective of this paper is to investigate the validity of these two methods to estimate peak load coefficients for heliostat configurations corresponding to the maximum load cases of the measured load fluctuation distributions.

2. Wind tunnel experiment method

2.1 Atmospheric boundary layer (ABL) generation and characterisation

Wind tunnel measurements were conducted in the atmospheric test section of the University of Adelaide wind tunnel using a base force balance equipped with a six-axis JR3 load cell and a heliostat model containing 24 Honeywell HSC series differential pressure sensors. Figure 1 shows the wind tunnel with a 3 m × 3 m cross-section and a 17 m development length to generate the atmospheric boundary layer (ABL) velocity and turbulence profiles.

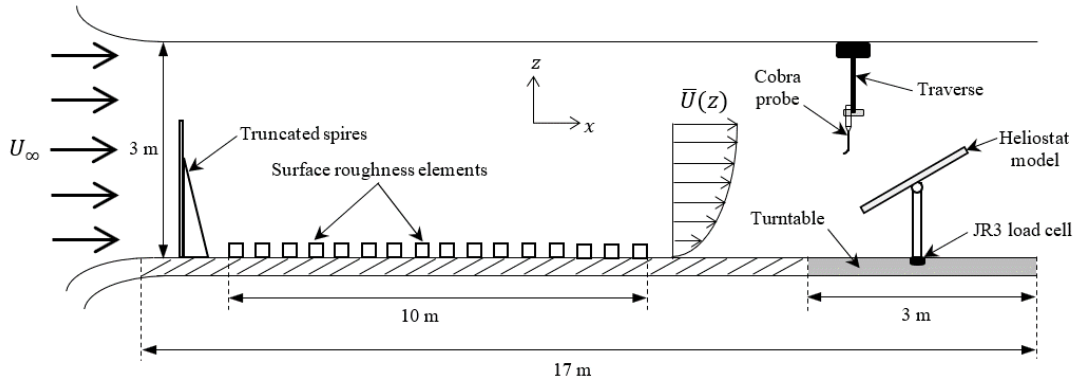


Figure 1. Schematic diagram showing experimental setup in the atmospheric test section of the University of Adelaide wind tunnel.

Flow measurements were sampled at 1 kHz using a multi-hole pressure probe mounted on a 2D traverse arm upstream of the heliostat model with an elevation axis height of 0.23 m within two simulated ABLs: BL1 with $U_{mean} = 9$ m/s and $I_u = 0.1$ and BL2 with $U_{mean} = 6.7$ m/s and $I_u = 0.145$ at the heliostat elevation axis height. Figure 2 shows the BL1 and BL2 mean velocity and turbulence intensity profiles compared with log law and ESDU 85020, respectively. The mean velocity and turbulence intensity profiles of BL1 show a good agreement with a logarithmic velocity profile and ESDU 85020 [7] turbulence intensity profiles of ABL with an aerodynamic surface roughness height of $z_0 = 0.002$ m. The longitudinal turbulence intensity profile for BL1 decreases with increasing height above the heliostat hinge height. BL2 mean

velocity and turbulence intensity profiles are well approximated by an ABL with $z_0 = 0.02$ m at heights below 0.5 m. These represent the turbulence intensities in a full-scale ABL ranging from a flat desert to an open country terrain.

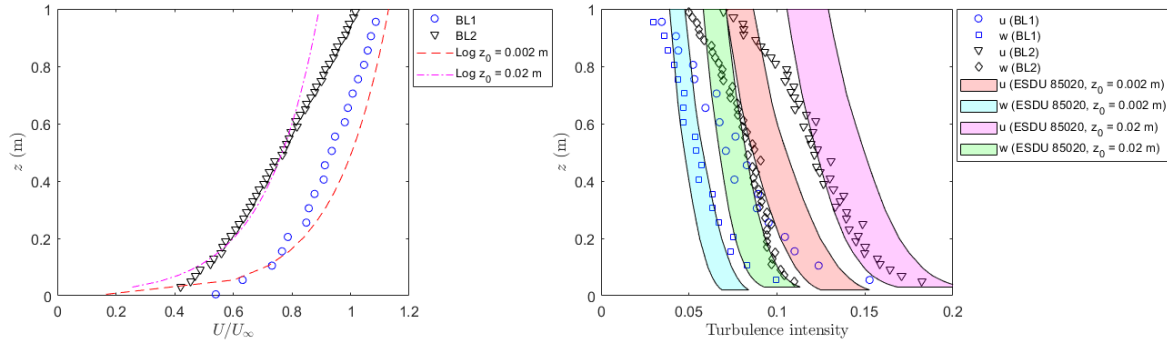


Figure 2. Characteristics of two atmospheric boundary layers (ABLs) generated in the wind tunnel: mean velocity profile compared with logarithmic profile (left), and turbulence intensity (right) profiles compared with ESDU 85020 [7] data with $\pm 10\%$ uncertainty bands.

2.2 Heliostat load measurement and characterisation

Figure 3 shows the heliostat model with rectangular surface of 0.53 m width and 0.33 m length and elevation axis height of 0.23 m, mounted on a force balance at its base. The force balance is a JR3 six-axis load cell with a nominal accuracy of $\pm 0.25\%$ of the full range of ± 100 N for x- and y-direction forces, ± 200 N for z-direction force and ± 12 Nm for moments in each of the three directions. The board-mounted pressure sensors have an operating range of ± 250 Pa. Base force and moment measurements were collected at 1 kHz sampling frequency for a duration of 120 seconds at a range of azimuth-elevation configurations of the heliostat model. The mean and root-mean-square (RMS) values of the load coefficients were calculated based on the time series of the base force and moment measurements.

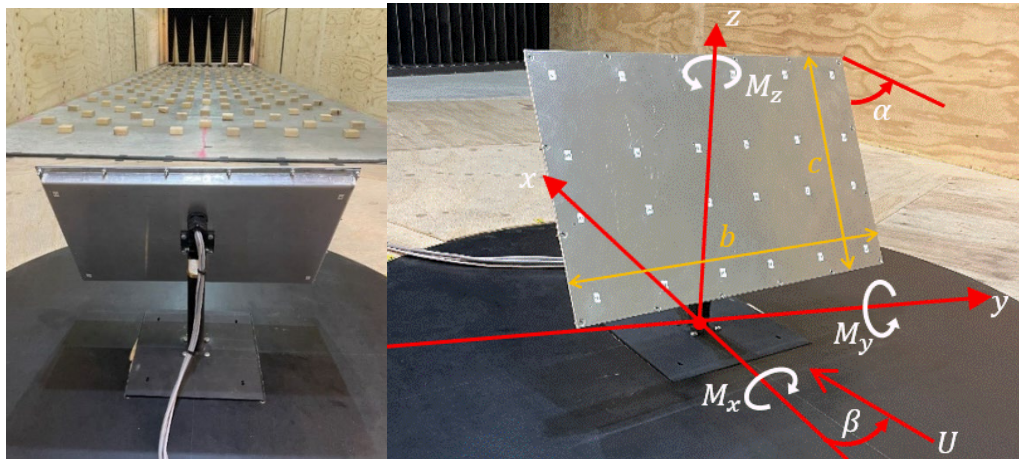


Figure 3. Experimental setup showing a rectangular pressure tapped heliostat model in the atmospheric test section of the University of Adelaide wind tunnel (left), and the coordinate system of JR3 load cell on force platform at base of heliostat model (right).

Wind load coefficients were calculated following the coordinate system in Figure 3(b) as

$$C_{Fx} = F_x / (0.5\rho U^2 A) \quad (3)$$

$$C_{Fz} = F_z / (0.5\rho U^2 A) \quad (4)$$

$$C_{Mz} = M_z / (0.5\rho U^2 A c) \quad (5)$$

$$C_{My} = My/(0.5\rho U^2 AH) \quad (6)$$

$$C_{MHy} = MHy/(0.5\rho U^2 Ac) = C_{My}(c/H) - C_{Fx} \quad (7)$$

Here ρ is air density, U is the mean velocity at the heliostat elevation axis height $H = 0.23$ m, $A = b \times c$ (width \times length) is the heliostat surface area. The hinge moment is calculated using the product of the centre of pressure and net force coefficient on the heliostat surface [8] as

$$C_{MHy} = (C_{Fn} \times l_{px}) / (0.5\rho U^2 Ac) \quad (8)$$

Here C_{Fn} is the net normal force calculated from the pressure distribution integrated over the surface of the heliostat and l_{px} is the distance along the length of the heliostat surface to the centre of pressure from the central elevation axis of the heliostat [8].

3. Results and Discussion

Figure 4 shows the peak drag and lift force coefficients calculated using the three-sigma and gust factor equations on the time series data. The peak values obtained by the integration of differential pressures over the heliostat surface and base force balance load cell measurements show a general agreement over the range of elevation angles, with average differences of 5% in lift and 20% in drag. The gust factor gives peak coefficients for maximum drag at $\alpha = 90^\circ$ that are 12% smaller in BL1 and 9% smaller in BL2 than those estimated by the three-sigma method. The opposite is observed for maximum lift at $\alpha = 30^\circ$, where the gust factor overestimates by 17% in BL1 and 28% in BL2 compared with the three-sigma. At $\alpha = 0^\circ$, the gust factor underestimates the peak lift coefficient by 50% in BL1 and BL2 due to the increased vertical amplitude responses in stow position.

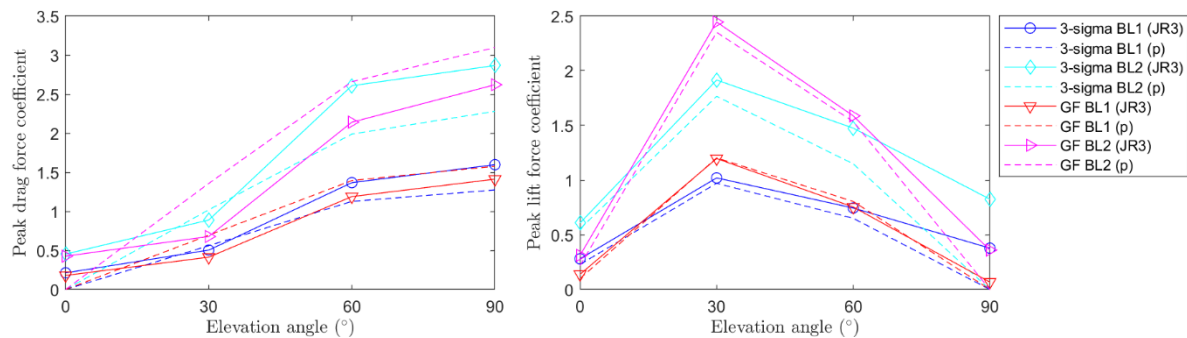


Figure 4. Comparison of the 3-sigma and gust factor statistical methods for calculation of peak load coefficients using integration of differential pressure sensors and base force balance JR3 load cell on a heliostat model at $\beta = 0^\circ$ in BL1 and BL2.

Figure 5 shows the statistical peak aerodynamic coefficients calculated using equations 3-7 on the heliostat model as a function of elevation angle α and azimuth angle β . The peak coefficients of drag force, lift force and overturning moment at $\beta = 180^\circ$ (Figure 5c) follow a similar variation with α to $\beta = 0^\circ$. The gust factor and three-sigma peak values are consistent in BL1, however there is some variation with increasing turbulence in BL2. For example, the gust factor predicts larger peak coefficients of drag force, lift force and overturning moment at $\beta = 0^\circ$ and $\beta = 180^\circ$. In contrast, the three-sigma peak values of both the hinge moment and azimuth moment coefficients tend to be larger than the gust factor peaks. The maximum value of hinge moment at $\beta = 60^\circ$ (Figure 5b) and $\beta = 180^\circ$ (Figure 5c) occurs at $\alpha = 60^\circ$, which is reflected with respect to $\alpha = 30^\circ$ maximum at $\beta = 0^\circ$ (Figure 5a).

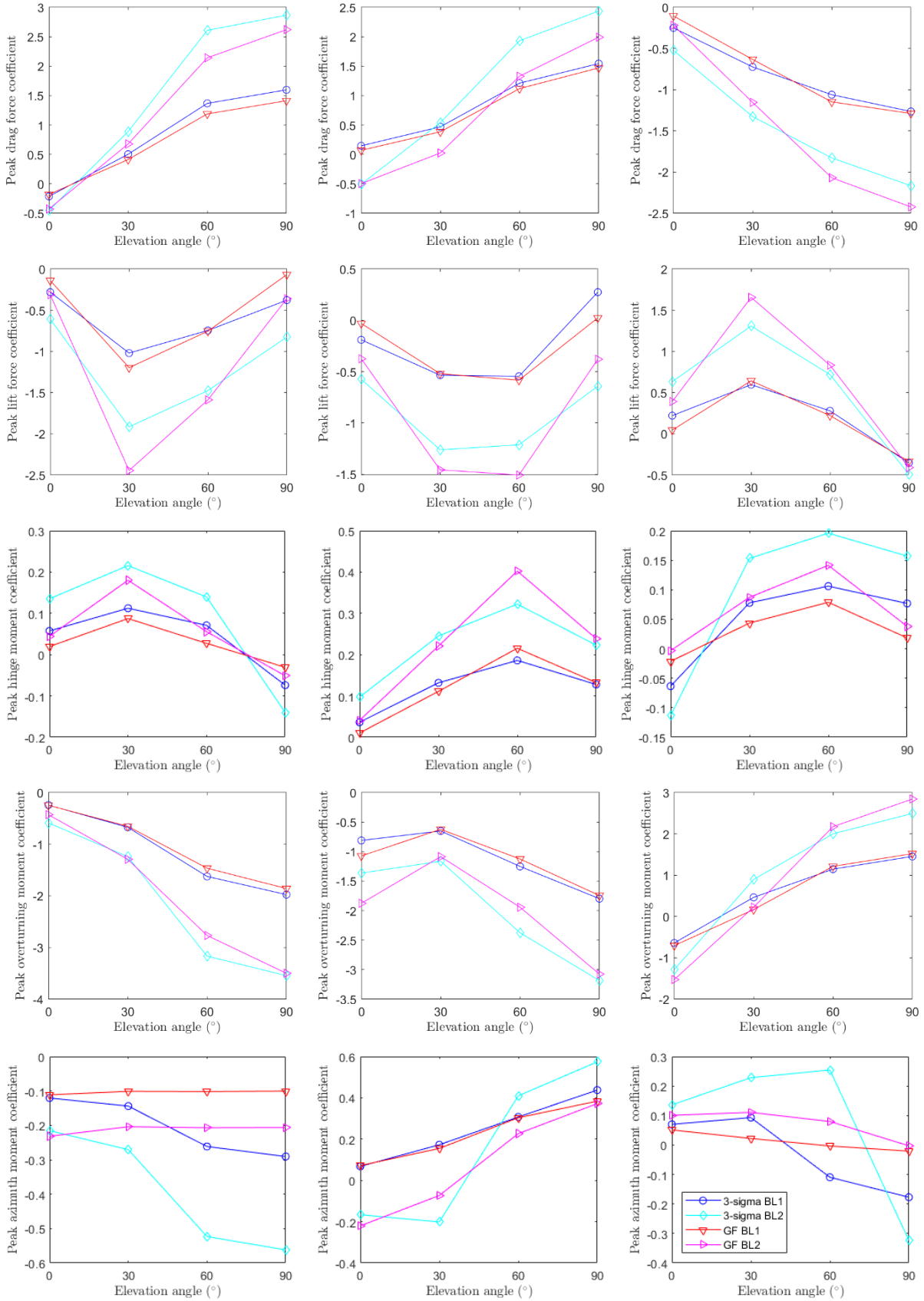


Figure 5. Comparison of the 3-sigma and gust factor statistical methods for calculation of peak load coefficients on a heliostat in BL1 and BL2 at (a) $\beta = 0^\circ$, (b) $\beta = 60^\circ$, (c) $\beta = 180^\circ$.

Figure 6 shows the distributions of the load coefficient fluctuations and a fitted Gaussian distribution for the maximum load cases of each coefficient in Figure 5. The distributions of all load coefficient fluctuations in BL1 show a good agreement through linear regression between the histogram and fitted Gaussian distribution ($R^2 > 0.95$) in the lower range below the mean value fluctuations. With increasing turbulence in BL2, the load distributions increase in skewness with a longer tail that is best approximated by a logarithmic regression between the histogram and fitted Gaussian distribution ($R^2 > 0.9$). Table 1 shows the percentage difference between the statistical peak predictions with reference to the measured maximum values. Three-sigma peak coefficients of the hinge moment, overturning moment and azimuth moment are 54%, 48% and 45% smaller, respectively, than the maximum values of the histogram distributions in BL2. This suggests that quasi-steady variation of the loads in gust factor estimates and following a Gaussian distribution in three-sigma estimates may underpredict the peak values of the maximum operating load cases influenced by vertical wind gust amplitudes in highly turbulent flows.

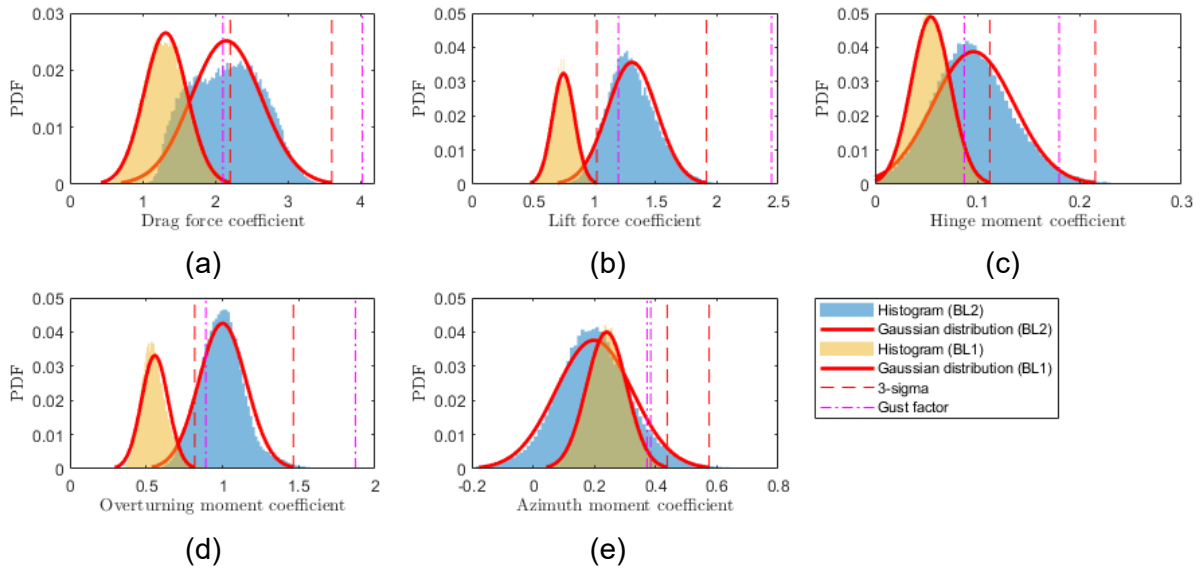


Figure 6. Distributions at maximum load cases compared with fitted Gaussian distribution and statistical peak values: (a) C_{Fx} at $\alpha = 90^\circ$, $\beta = 0^\circ$, (b) C_{Fz} at $\alpha = 30^\circ$, $\beta = 0^\circ$, (c) C_{MHy} at $\alpha = 30^\circ$, $\beta = 0^\circ$, (d) C_{My} at $\alpha = 90^\circ$, $\beta = 0^\circ$, (e) C_{Mz} at $\alpha = 90^\circ$, $\beta = 60^\circ$.

Table 1. Percentage difference between statistical peak and maximum values in BL1, BL2.

Statistical method	Drag force	Lift force	Hinge moment	Overturning moment	Azimuth moment
Three-sigma	-7, -7	-14, -24	-88, -54	-26, -48	-31, -45
Gust factor	-11, +5	+3, +3	-141, -85	-16, -16	-49, -124

Figure 7 shows the distributions of the centre of pressure position l_{px}/c on the heliostat surface of chord length c in the windward direction (Figure 3b). At $\beta = 0^\circ$ in BL1 and BL2 (Figure 7a,d) in BL2, the centre of pressure position moves from the central elevation axis at $\alpha = 60^\circ$ and 90° toward the leading (windward) edge of the heliostat at $\alpha = 0^\circ$. The distribution of l_{px}/c is within ± 0.1 and closely follows a Gaussian distribution at $\alpha = 30^\circ$, 60° and 90° . In contrast at $\alpha = 0^\circ$, l_{px}/c is highly skewed toward an inverse Weibull distribution with a mode of -0.3 and peak of approximately -0.4. The centre of pressure position at $\beta = 60^\circ$ in BL1 and BL2 (Figure 7b,e) is shifted closer to the central elevation axis at $\alpha = 0^\circ$ but is shifted further from the central elevation axis toward the leading edge at $\alpha = 30^\circ$, 60° and 90° in comparison to $\beta = 0^\circ$. At $\beta = 180^\circ$ in BL1 and BL2 (Figure 7c,f), l_{px}/c is reflected about the central elevation axis in stow and operating angles compared to $\beta = 0^\circ$ toward the heliostat trailing edge, with mode of 0.3 and peak of 0.4 in stow and larger l_{px}/c at $\alpha = 60^\circ$ compared to $\alpha = 30^\circ$.

Figure 8 shows the distributions of the hinge moment calculated using the centre of pressure position in Figure 7 and the net force normal to the surface from the pressure distribution at different elevation and azimuth angles. The hinge moment at operating angles shows a large variation with azimuth angle, where maximum values at $\alpha = 30^\circ$ for $\beta = 0^\circ$ in BL1 and BL2 (Figure 7a,d) are not reflected at $\beta = 60^\circ$ and $\beta = 180^\circ$ where maximum values occur at $\alpha = 60^\circ$. The hinge moment distribution shows non-Gaussian characteristics in stow position at all β , where instantaneous peaks are correlated to the centre of pressure position due to the unsteady pressure distribution over the heliostat surface in the ABL.

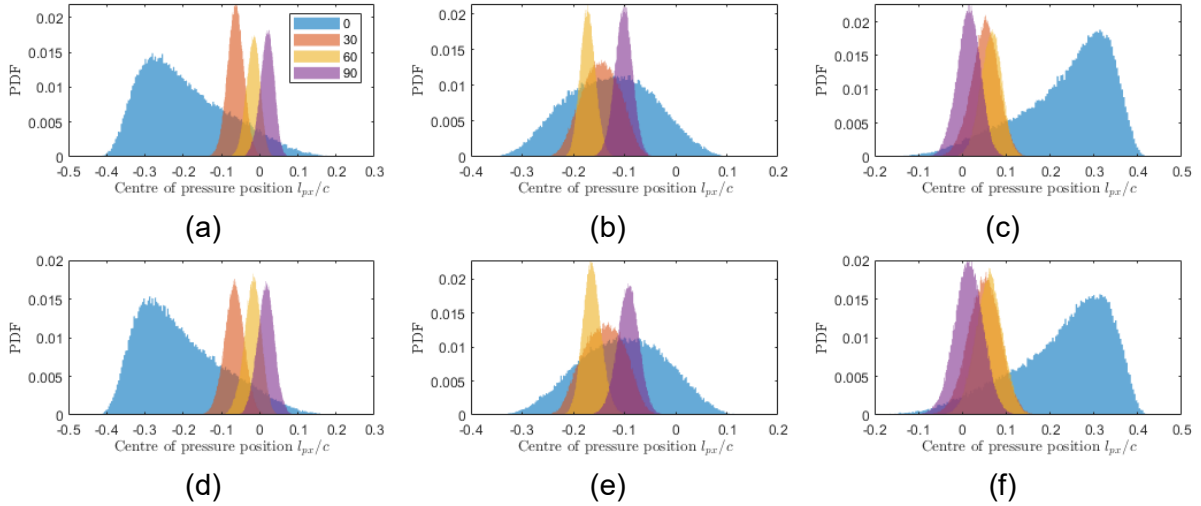


Figure 7. Distribution of centre of pressure position l_{px}/c as a function of elevation angle of the heliostat model in BL1 at (a) $\beta = 0^\circ$, (b) $\beta = 60^\circ$, (c) $\beta = 180^\circ$, and in BL2 at (d) $\beta = 0^\circ$, (e) $\beta = 60^\circ$, (f) $\beta = 180^\circ$.

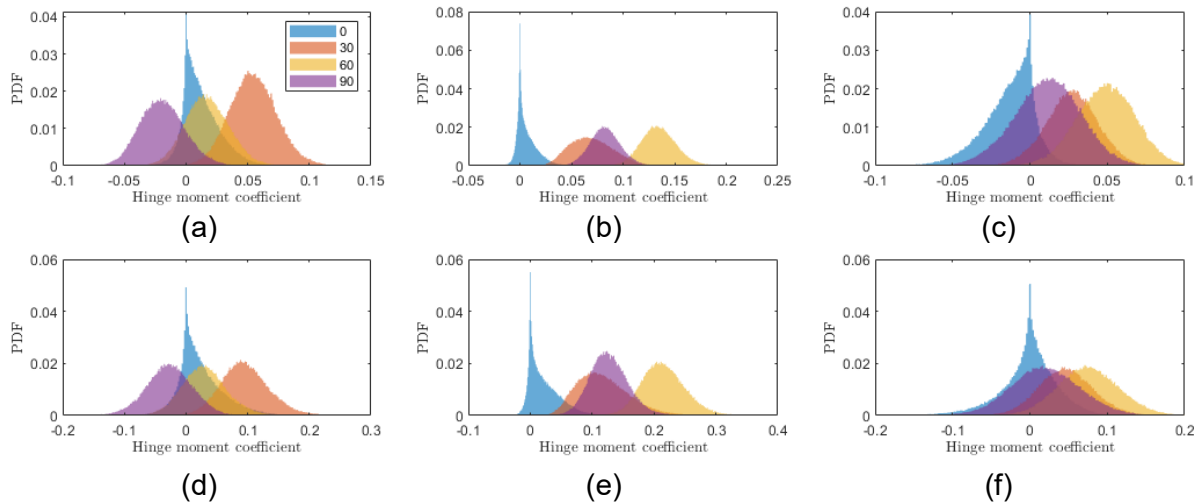


Figure 8. Distribution of hinge moment coefficient C_{MHy} as a function of elevation angle of the heliostat model in BL1 at (a) $\beta = 0^\circ$, (b) $\beta = 60^\circ$, (c) $\beta = 180^\circ$, and in BL2 at (d) $\beta = 0^\circ$, (e) $\beta = 60^\circ$, (f) $\beta = 180^\circ$.

4. Conclusions

This paper investigated the distributions of base force balance and surface pressure load fluctuations on a rectangular heliostat surface in two atmospheric boundary layer turbulence profiles. Comparison of statistical methods for peak wind load predictions with measured maximum values shows that the gust factor overestimates the maximum operating forces and provides a more accurate prediction of maximum operating forces and overturning moments

than three-sigma. The gust factor significantly underestimates the maximum hinge moment and azimuth moments as the peak factor is a linear function of longitudinal turbulence intensity representing the magnitude of horizontal wind gust velocity amplitude. Distributions of stow and operating hinge moments and azimuth moments are non-Gaussian due to unsteady centre of pressure variations. The three-sigma approach is therefore recommended in these cases for any heliostat size, and the frequency and amplitude of the vertical wind velocity component must be considered for accurate peak load predictions.

Data availability statement

Data in the article can be accessed by contacting the corresponding author.

Author contributions

Matthew Emes contributed to conceptualization, funding acquisition, data curation, formal analysis, investigation, methodology, software, visualization and writing original draft. Bruce Leslie contributed to conceptualization, review and editing. Maziar Arjomandi contributed to conceptualization, methodology, funding acquisition, review and editing.

Competing interests

The authors declare no competing interests.

Funding

The work is funded by the Australian Renewable Energy Agency (ARENA) Grant 1-SRI002 as part of the Australian Solar Thermal Research Institute (ASTRI) P11 project.

Acknowledgement

The authors acknowledge the mechanical and electronic workshops at the University of Adelaide for their technical support in manufacturing prototypes and instrumentation. The authors also acknowledge PhD student Matthew Marano for assistance with collecting data.

References

1. J. A. Peterka and R. G. Derickson, Wind load design methods for ground-based heliostats and parabolic dish collectors (Sandia National Laboratories, Albuquerque, New Mexico, 1992), SAND92-7009. <https://doi.org/10.2172/7105290>
2. M. Emes, A. Jafari and M. Arjomandi, Wind load design considerations for the elevation and azimuth drives of a heliostat, AIP Conference Proceedings 2303, 030013 (2020). <https://doi.org/10.1063/5.0028609>
3. M. J. Emes, A. Jafari, J. Coventry and M. Arjomandi, The influence of atmospheric boundary layer turbulence on the design wind loads and cost of heliostats, Solar Energy 207, 796-812 (2020). <https://doi.org/10.1016/j.solener.2020.07.022>
4. E. Simiu and R. H. Scanlan, Wind effects on structures: fundamentals and applications to design, John Wiley & Sons, 1996.
5. N. J. Cook, Designers guide to wind loading of building structures. Part 1, 1986.
6. J. D. Holmes, A. C. Allsop and J. D. Ginger, Gust durations, gust factors and gust response factors in wind codes and standards, Wind and Structures 19, 339-352 (2014). <https://doi.org/10.12989/was.2014.19.3.339>
7. ESDU 85020, Characteristics of atmospheric turbulence near the ground, Part II: single point data for strong winds, Engineering Sciences Data Unit, London, 2001.
8. M. J. Emes, A. Jafari, F. Ghanadi and M. Arjomandi, Hinge and overturning moments due to unsteady heliostat pressure distributions in a turbulent atmospheric boundary layer, Solar Energy 193, 604-617 (2019). <https://doi.org/10.1016/j.solener.2019.09.097>